

Article

A Novel Method for Hyperspectral Mineral Mapping Based on Clustering-Matching and Nonnegative Matrix Factorization

Zhongliang Ren ¹, Qiuping Zhai ² and Lin Sun ^{1,*}

¹ College of Geodesy and Geomatics, Shandong University of Science and Technology, Qingdao 266590, China; 201881020025@sdust.edu.cn

² Shandong Provincial Key Laboratory of Water and Soil Conservation and Environmental Protection, School of Resource and Environmental Sciences, Linyi University, Linyi 276000, China; zhaiqiuping@lyu.edu.cn

* Correspondence: sunlin@sdust.edu.cn; Tel.: +86-532-8803-2922

Abstract: The emergence of hyperspectral imagery paved a new way for rapid mineral mapping. As a classical hyperspectral classification method, spectral matching (SM) can automatically map the spatial distribution of minerals without the need for selecting training samples. However, due to the influence of noise, the mapping accuracy of SM is usually poor, and its per-pixel matching method is inefficient to some extent. To solve these problems, we propose an unsupervised clustering-matching mapping method, using a combination of k-means and SM (KSM). First, nonnegative matrix factorization (NMF) is used and combined with a simple and effective NMF initialization method (SMNMF) for feature extraction. Then, k-means is implemented to get the cluster centers of the extracted features and band depth, which are used for clustering and matching, respectively. Finally, dimensionless matching methods, including spectral angle mapper (SAM), spectral correlation angle (SCA), spectral gradient angle (SGA), and a combined matching method (SCGA) are used to match the cluster centers of band depth with a spectral library to obtain the mineral mapping results. A case study on the airborne hyperspectral image of Cuprite, Nevada, USA, demonstrated that the average overall accuracies of KSM based on SAM, SCA, SGA, and SCGA are approximately 22%, 22%, 35%, and 33% higher than those of SM, respectively, and KSM can save more than 95% of the mapping time. Moreover, the mapping accuracy and efficiency of SMNMF are about 15% and 38% higher than those of the widely used NMF initialization method. In addition, the proposed SCGA could achieve promising mapping results at both high and low signal-to-noise ratios compared with other matching methods. The mapping method proposed in this study provides a new solution for the rapid and autonomous identification of minerals and other fine objects.

Citation: Ren, Z.; Zhai, Q.; Sun, L. A Novel Method for Hyperspectral Mineral Mapping Based on Clustering-Matching and Nonnegative Matrix Factorization. *Remote Sens.* **2022**, *14*, 1042. <https://doi.org/10.3390/rs14041042>

Academic Editors: Olga Sykioti and Konstantinos Koutroumbas

Received: 25 December 2021

Accepted: 19 February 2022

Published: 21 February 2022

Publisher's Note: MDPI stays neutral with regard to jurisdictional claims in published maps and institutional affiliations.



Copyright: © 2022 by the authors. Licensee MDPI, Basel, Switzerland. This article is an open access article distributed under the terms and conditions of the Creative Commons Attribution (CC BY) license (<https://creativecommons.org/licenses/by/4.0/>).

Keywords: hyperspectral mineral mapping; clustering; spectral matching; nonnegative matrix factorization

1. Introduction

Minerals, as a nonrenewable resource, play an important role in the survival and development of human society. For example, kaolin and muscovite can be used as ceramic and refractory materials [1,2]. Food production requires mineral fertilizers, such as nitrogen, phosphorus, and potassium [3,4]. Montmorillonite powder can be used to treat chronic diarrhea [5]. Mapping these mineral resources is a prerequisite for their utilization. The traditional mineral mapping method uses the experience of geologists and laboratory equipment to identify minerals. The large-scale application of this method is time-consuming and laborious. Remote sensing technology, especially hyperspectral remote sensing, makes it possible to realize a wide area of mineral mapping [6].

In fact, mineral mapping is one of the most successful applications of hyperspectral remote sensing [7] because hyperspectral imagery usually has high spectral resolution

and hundreds of continuous spectral bands covering the range from the visible to shortwave infrared spectra, which can serve to identify various minerals and map their spatial distribution [8]. The rationale behind hyperspectral mineral mapping is that mineral species have diagnostic spectral absorption features from 20 to 40 nm full-width at half-maximum [9]. The spectral resolutions of commonly used hyperspectral images are usually around 10 nm [10], thus making the rapid identification and mapping of surface minerals possible.

Over the past decades, different hyperspectral mineral mapping methods have been developed, including supervised classification [11], spectral unmixing [12], and spectral matching (SM) [13]. Supervised methods can provide promising classification performance when training samples are sufficient [14]. However, the selection and evaluation of training samples are time-consuming and very difficult for fine objects, such as minerals and vegetation [15]. Also, for hyperspectral imagery, the small ratio between the number of training samples and the available number of spectral features usually makes the supervised training process prone to overfitting (i.e., the Hughes phenomenon) [16,17]. Spectral unmixing can provide the abundance of various minerals in a pixel. Nevertheless, endmember extraction, the key step of spectral unmixing, usually assumes the existence of pure pixels or has quite high computational complexity [18–20]. SM matches the spectrum of each pixel with a spectral library and then classifies the pixel according to its greatest similarity with a category [21]. In fact, the emergence of imaging spectrometers and SM provides the possibility to automatically obtain classification information from remote sensing images [22]. However, although SM based on the whole waveform features is simple without complex analysis of the spectrum or adjustment of thresholds, the mineral mapping results of SM are generally fragmentary because of its sensitivity to noise and the requirement of a high signal-to-noise ratio (SNR) of hyperspectral imagery [23,24]. Moreover, since hyperspectral images usually have hundreds of thousands or even more pixels with a high spectral resolution, the per-pixel matching method of SM is inefficient to some extent.

Another commonly used classification algorithm that does not require training samples and endmember extraction is clustering (i.e., unsupervised classification), which groups similar data points into the same cluster [25]. Clustering has been widely used in data mining, machine learning, and image classification [26,27]. In fact, clustering and SM can complement each other in hyperspectral classification. On the one hand, considering that the clustering result only reflects the spatial distribution of different clusters without giving specific types, the final classification results can be obtained by matching the cluster centers with a spectral library. On the other hand, since the noise in signals can be removed to a certain extent by averaging [28–32], the de-noised cluster centers can be obtained by averaging their corresponding pixels in the original or enhanced hyperspectral image. Moreover, the matching between the cluster centers and spectral library is block-wise rather than pixel-wise. Thus, the fragmentation of the mapping results of SM may be reduced by matching the de-noised cluster centers with a spectral library. Furthermore, since the number of cluster centers (K) is usually much fewer than the pixel number of a hyperspectral image, the combination of clustering and SM (i.e., clustering-matching) has great potential to improve the mineral mapping efficiency of SM without destroying its nonsupervision. Therefore, clustering-matching, a novel, unsupervised, hyperspectral classification method, was proposed to address the accuracy and efficiency of SM in mineral mapping.

Since high dimensionality and correlation of hyperspectral image will reduce the clustering efficiency and accuracy [33], feature extraction should be carried out first before clustering-matching. In general, there are linear and nonlinear hyperspectral feature extraction methods. Considering that the former has lower computational complexity and memory cost [34,35], linear features will be used for clustering. Nonnegative matrix factorization (NMF), proposed by Lee and Seung [36], is an effective algebraic method in extracting linear features for clustering [37]. Compared with other feature extraction

methods, NMF can preserve the majority of the original image structure and guarantee the nonnegative nature of both the base and coefficient matrix [38]. However, since NMF is a nonconvex optimization problem, its feature extraction results depend heavily on the performance of initialization methods [39]. In fact, NMF can be used not only for dimensionality reduction, but also for soft clustering [40]. Based on this, the current study proposes a simple and effective initialization method from the perspective of NMF clustering.

In this study, the clustering-matching mapping method had three steps: First, NMF was carried out to extract the spectral features that reflect the distribution of various minerals. Second, clustering was implemented based on the extracted features and the de-noised cluster centers, from which the enhanced hyperspectral image can be calculated using the final clustering result or directly obtained during the clustering process. Finally, three common matching methods and a combined matching method were used to match the de-noised cluster centers with a mineral spectral library to obtain the final mineral mapping results.

2. Materials

2.1. Study Area

The study area, Cuprite (Figure 1a), is located approximately 200 km northwest of Las Vegas, Nevada, and is separated into eastern and western regions by US Highway 95. Cuprite is ideal for geologic mapping, as different mineral types are exposed to very little vegetation cover, and it has been used as a geologic remote-sensing test site since the early 1980s [41,42]. Figure 1b exhibits the mineral distribution map of Cuprite derived from the United States Geological Survey (USGS), which was developed by Clark according to the vibrational absorption features of minerals [43]. Six mineral types, including alunite, calcite, kaolinite, muscovite, chalcedony, and montmorillonite have been discovered in this area [44].

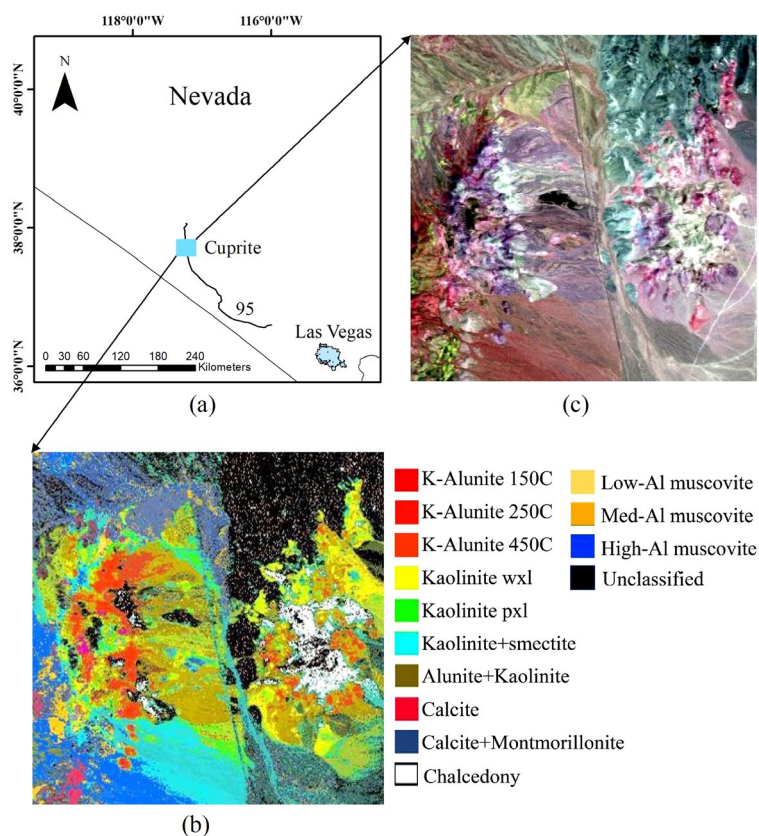


Figure 1. Study area and data: (a) location map; (b) mineral distribution map from USGS; and (c) AVIRIS image.

2.2. Datasets

2.2.1. Hyperspectral Data

The study data were derived from airborne visible/infrared imaging spectrometer (AVIRIS), which covers a spectral range of 0.4–2.5 μm with a spectral resolution of 10 nm and 224 contiguous bands [45]. The AVIRIS image (Figure 1c) used in this study has 50 bands covering the shortwave infrared of 2.0–2.5 μm , with a spatial resolution of 20 m, consisting of 350 lines and columns. This image was chosen because the spectral range of 2.0–2.5 μm covers the spectral features of many alteration minerals [46]. Furthermore, this image has been corrected by an empirical flat field optimized reflectance transformation [47]. To assess the mapping accuracy, registration between the AVIRIS image and the mineral distribution map has been performed, and the root-mean-square error was less than 1 pixel.

2.2.2. Spectral Library

The spectral library contains the reflectivity of various objects measured by the spectrometer and plays an important role in the quick and accurate identification of fine objects. This study uses the USGS mineral spectral library for matching, which has 481 mineral spectra [48]. Each spectral curve has 420 bands covering a spectral range of 0.4–2.6 μm . It can be seen in Figure 2 that, although the spectral absorption features of the six Cuprite minerals are mainly distributed in the spectral range of about 1.4–2.5 μm , they are quite different, which is the prerequisite for hyperspectral mineral mapping.

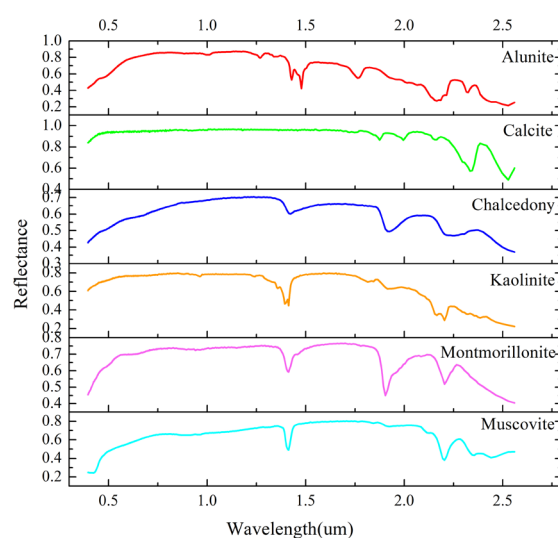


Figure 2. The spectral curves of the Cuprite minerals in the USGS spectral library.

3. Methodology

3.1. Spectral Preprocessing

As SM requires the hyperspectral image and spectral library to have the same spectral range and resolution, spectral resampling of the USGS mineral spectral library was performed using the environment for visualizing images before matching. Moreover, band depth (BD) was used to enhance the spectral absorption differences of various minerals [49]. The calculation of BD includes three steps: (1) connecting the extreme points of the spectral curve to form the envelope; (2) dividing the original spectrum by the envelope to generate the continuum removal [50]; and (3) subtracting the continuum removal from 1 to obtain the BD.

$$SL = \frac{R_e - R_s}{\lambda_e - \lambda_s} \quad (1)$$

$$BD = 1 - \frac{R_i}{R_s + SL \cdot (\lambda_i - \lambda_s)} \quad (2)$$

where R is the reflectance; λ is the wavelength; SL represents the slope; i is the band index; and e and s are the ending and starting points of the segmented straight lines of the envelope, respectively. As shown in Figure 3, the envelope completely wraps the original spectral curve, and the BD greatly enhances the spectral absorption depth of muscovite.

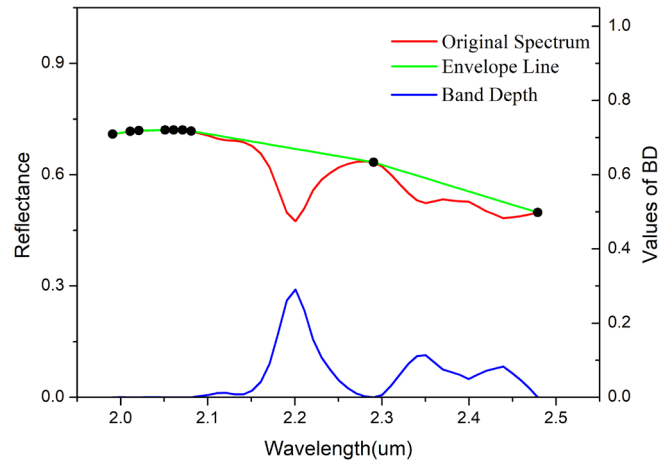


Figure 3. Spectral curves of muscovite of USGS mineral spectral library after spectral preprocessing.

3.2. Clustering-Matching

Figure 4 shows a flowchart of the clustering-matching procedure, which includes three steps: (i) extracting the spectral features that can well reflect the distribution of various minerals; (ii) clustering based on the extracted spectral features; and (iii) matching the de-noised cluster centers with the USGS mineral spectral library by dimensionless matching methods.

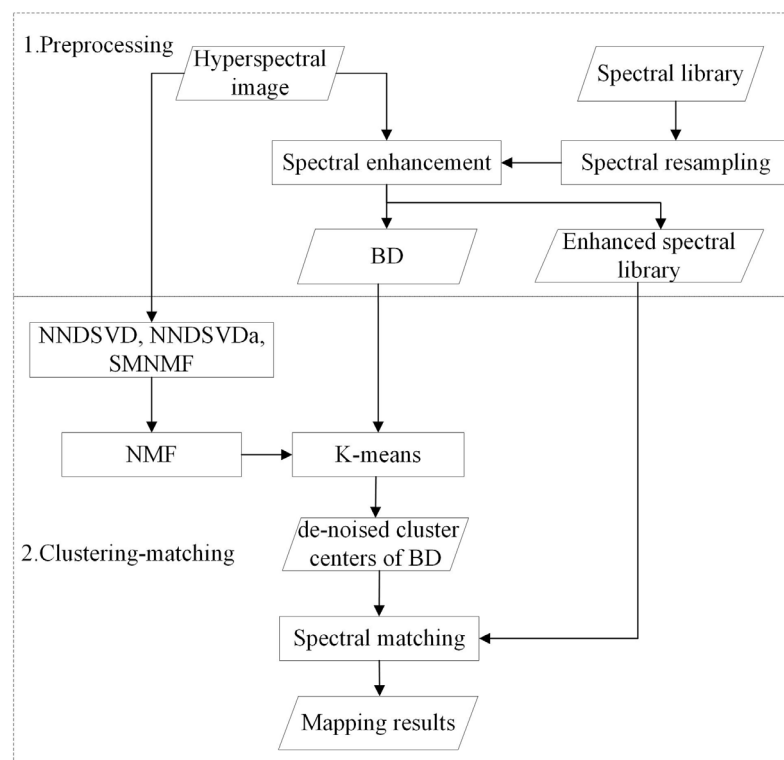


Figure 4. Flowchart of the clustering-matching procedure.

3.2.1. Feature Extraction

The main idea of NMF is to discover two low-rank factor matrices to approximate an input large-dimensional nonnegative matrix $V \in R_+^{m \times n}$ with the following objective function [51]:

$$\min_{W \in R_+^{m \times r}, H \in R_+^{r \times n}} \|V - WH\|_F^2 \quad \text{s. t. } W, H \geq 0 \quad (3)$$

where $\|\cdot\|_F$ denotes the Frobenius norm; from the perspective of dimensionality reduction, W and H are the basis and coefficient matrix, respectively; m and n are the pixel and band number, respectively; r is the factorization rank. All elements of W and H must be nonnegative. Alternating least squares (ALS) [52,53] was used for solving this objective function. The update rule of ALS is described as follows, and the maximum number of steps allowed is set as 1000:

$$H \leftarrow (W^T W)^{-1} W^T V \quad \text{s. t. } H \geq 0 \quad (4)$$

$$W \leftarrow V H^T (H H^T)^{-1} \quad \text{s. t. } W \geq 0 \quad (5)$$

Since NMF is a nonconvex optimization problem, there is no guarantee that the W and H matrices are optimally determined, which means that the different initial values of W and H may provide different NMF results. Therefore, particular emphasis has to be placed on NMF initialization. At present, random initialization, clustering-based initialization [54], and matrix factorization initialization [55] can be used to obtain the initial W and H matrices. Among the three initialization methods, only matrix factorization contains no randomization. Nevertheless, except for NMF, other matrix factorization algorithms, such as singular value decomposition (SVD) [56] and independent component analysis [57], usually produce negative values, which violates the nonnegative constraint of NMF.

In fact, NMF can not only be used for feature extraction, but it also has a wide application in clustering [58,59]. From the perspective of clustering, W is equivalent to the cluster division, and H is the centroid set, in which the pixel spectra of various minerals should well reflect their spectral absorption differences. For hyperspectral images, these representative pixels in H can be obtained by matching with the spectral library. Based on this, an NMF initialization method using SM, called SMNMF, was proposed. Firstly, r was set as 6, which is the mineral type number of the AVIRIS image. Then, H was initialized with the pixels most similar to each mineral type. Finally, the initial W matrix was calculated using Equation (7):

$$H = \{p \mid p = \arg \min \text{SMF}(V, M)\} \quad \text{s. t. } H \geq 0 \quad (6)$$

$$W = V/H \quad \text{s. t. } W \geq 0 \quad (7)$$

where SMF is a similarity measurement function and is specified as the combined matching method in this study, which will be introduced later; M represents the spectra of the six mineral types and is obtained from the USGS mineral spectral library; and p is a pixel that is most similar to one mineral type. Since the H matrix obtained by SM is unique, SMNMF can also obtain a definite initial solution without producing negative values.

The most widely used NMF initialization method, Nonnegative Double Singular Value Decomposition (NNDSD) and its slightly modified variant (NNDSDa) [56,60], were used for comparison with SMNMF in mineral mapping. It can be seen from Figure 5 that the NMF features obtained based on SMNMF and NNDSDa can reflect the distribution of various minerals to a certain extent, while the brightness of the feature image initialized by NNDSD is generally low. This is the case because, in order to keep the matrix nonnegative, NNDSD initializes NMF only using the positive section of the singular vectors, and the negative elements are set to zeros, indicating that the initial W and H matrices extracted by NNDSD are likely to contain many zeros. Therefore, NNDSD is only suited for the sparse case and may lead to a worse error than random initialization

in the dense case [60]. To address this problem, NNDSVDa sets all zeros to the average of all elements of an image. However, this ensemble average is unreasonable to some extent because, if the pixel number of various types varies greatly, some types with fewer pixels may be lost in the classification.

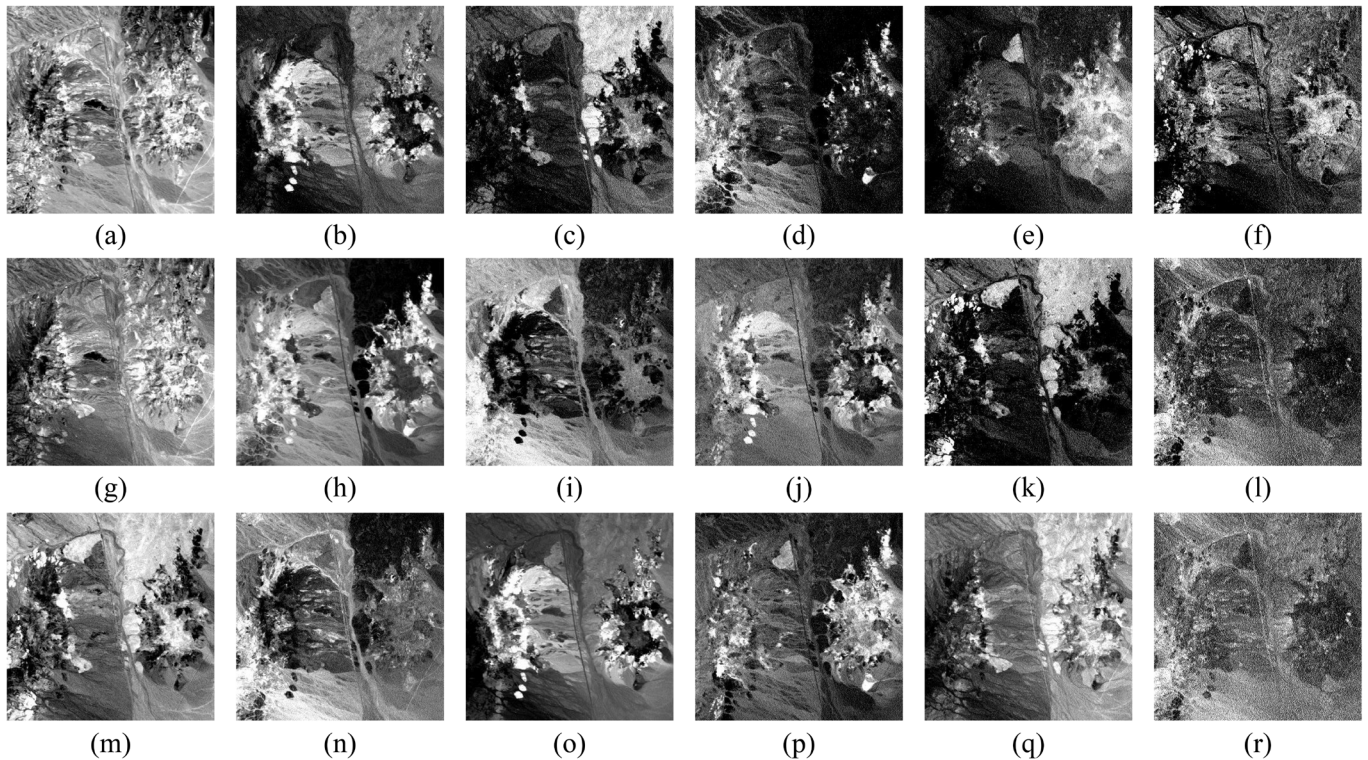


Figure 5. Spectral features of the AVIRIS image extracted by NMF: (a–f) are the NMF features initialized by NNDSVD; (g–l) are the NMF features initialized by NNDSVDa; and (m–r) are the NMF features initialized by SMNMF.

3.2.2. Clustering

To date, an abundant number of clustering algorithms have been developed. In this study, *k*-means was used for clustering for two reasons. On the one hand, it is obvious that the clustering complexity will affect the mapping efficiency of clustering-matching. If the complexity and memory requirements of the clustering algorithm are high, such as in the case of spectral clustering and affinity propagation [61,62], the mapping efficiency of clustering-matching will not be significantly improved, even if *K* is far less than the pixel number. Therefore, *k*-means, one of the ten classical algorithms in data mining, was used for clustering-matching due to its speed and simplicity. On the other hand, since *k*-means updates the cluster centers by averaging, the de-noised cluster centers can be directly obtained when the clustering iteration stops, and there is no need to use the final clustering result to average the corresponding pixels from the enhanced hyperspectral image. In this study, KSM is short for the combination of *k*-means and SM, and the KSM mapping methods based on NNDSVD, NNDSVDa, and SMNMF are called NKSM, NAKSM, and SKSM, respectively.

K-means is an iterative clustering algorithm. Its objective function is to minimize the sum of the squared errors (SSE) [63]:

$$SSE(C) = \sum_{i=1}^K \sum_{j=1}^{N_i} \|x_{ij} - c_i\|_F^2 \quad (8)$$

where c_i is one cluster center; N_i is the pixel number of c_i ; and x_{ij} is one pixel of c_i . Unlike the traditional *k*-means, KSM has two cluster centers during the clustering process. One

cluster center, called Center1, is calculated from the extracted features and used to judge whether the clustering iteration should be stopped. Another cluster center, called Center2, is calculated from the BD and used to match with the enhanced USGS spectral library to get the mineral mapping results. Generally, k-means has four steps: (1) initialization, where K is set, and Center1 and Center2 are selected randomly; (2) division, where each pixel in the feature image is divided into its nearest cluster center, and a category index of each pixel can be obtained; (3) updating, where Center1 and Center2 are respectively updated by calculating the average of pixels in the feature image and the BD based on the category index; and (4) iteration, where the algorithm returns to step 2 until Center1 does not change. In this way, when k-means stops iterating, the de-noised cluster centers of the BD (i.e., Center2) can be obtained directly.

The clustering results of k-means are limited by the indeterminacy of K. In this study, K was set as 481, namely the number of spectra in the USGS spectral library, which is far greater than the mineral type number of the AVIRIS image because, as K increases, the intra-cluster similarity of each cluster also increases, resulting in the decrease of SSE. That is, in theory, a larger K is conducive to improving the mineral mapping accuracy of KSM. In addition, the clustering results of k-means depend heavily on the initial cluster centers [64], which means different initial cluster centers may lead to different clustering-matching results. Therefore, to comprehensively analyze the performance of KSM in mineral mapping, the initial cluster centers should cover all pixels in the AVIRIS image as far as possible. Thus, the k-means clustering was performed 254 times, and 481 different initial cluster centers were randomly selected for each clustering. In other words, a total of 122,174 (i.e., 254 * 481) nonrepeating pixels were used as the initial cluster centers, covering almost the entire AVIRIS image. Therefore, 254 clustering-matching mapping results were generated for the AVIRIS image.

3.2.3. Matching

Since the clustering result solely reflects the mineral distribution without providing specific mineral types, four dimensionless matching methods, including spectral angle mapper (SAM), spectral correlation angle (SCA), spectral gradient angle (SGA), and a combined matching method, were used to match Center2 with the enhanced USGS mineral spectral library to obtain the final mineral mapping results.

SAM measures the similarity of two spectral vectors by calculating the cosine angle between them [65]:

$$SAM = \arccos \left(\frac{\sum_{i=1}^n V_{ti} * V_{ri}}{\|V_t\| \cdot \|V_r\|} \right) \quad (9)$$

where V_t and V_r represent the target and reference spectral vectors, respectively. SAM is invariant to scalar multiplication. SCA uses the Pearson correlation coefficient for matching:

$$SCA = \arccos \left(\left(\frac{\sum_{i=1}^n (V_{ti} - \bar{V}_t) * (V_{ri} - \bar{V}_r)}{\|V_t - \bar{V}_t\| \cdot \|V_r - \bar{V}_r\|} + 1 \right) / 2 \right) \quad (10)$$

where \bar{V}_t and \bar{V}_r are the mean values of V_t and V_r , respectively. SGA uses the gradient of two spectral vectors to calculate their shape similarity [66]:

$$SG_t = (V_{t2} - V_{t1}, V_{t3} - V_{t2}, \dots, V_{tn} - V_{t(n-1)}) \quad (11)$$

$$SG_r = (V_{r2} - V_{r1}, V_{r3} - V_{r2}, \dots, V_{rn} - V_{r(n-1)}) \quad (12)$$

$$SGA = \arccos \left(\frac{\sum_{i=1}^{(n-1)} SG_{ti} * SG_{ri}}{\|SG_t\| \cdot \|SG_r\|} \right) \quad (13)$$

where SG_t and SG_r are the spectral gradient vectors of V_t and V_r , respectively.

In fact, as can be seen from Equations (9), (10), and (13), SCA and SGA are both variants of SAM. Compared with SAM, SCA can distinguish between positive and negative correlations, while SGA provides the advantage of considering slope changes within the spectral vector [67]. However, since the fluctuation of the spectral curve caused by noise poses a great influence on the slope changes, the mapping results of SGA may not be ideal when SNR is lower, while SCA is less sensitive to the spectral changes caused by noise through decentralization. Therefore, to measure the correlation and shape similarity of two spectral curves simultaneously, this study proposes a combined matching method called SCGA, which combines SCA and SGA according to the following equation:

$$SCGA = \text{sqrt}(SCA^2 + SGA^2) \quad (14)$$

The smaller the value of the four matching methods, the greater the similarity between the target and reference spectral vectors.

3.2.4. Accuracy Assessment

In this study, the overall accuracy (OA) [68] is used to evaluate the mineral mapping performances of SM and KSM. OA is the probability that the classification results are consistent with the actual results. It considers the number of correctly classified pixels in the diagonal direction of the confusion matrix.

$$OA = \sum_{j=1}^m q_{jj}/N \quad (15)$$

Here, m is the number of mineral types; q_{jj} is the sum of the confusion matrix diagonal; and N is the total number of samples.

4. Results

In this study, there are four mapping methods including SM, NKSM, NAKSM, and SKSM. Each mapping method uses SAM, SCA, SGA, and SCGA for matching. Thus, the combination of the mapping and matching methods constitutes 16 classifiers, including SM-SAM, SM-SCA, SM-SGA, SM-SCGA, NKSM-SAM, NKSM-SCA, NKSM-SGA, NKSM-SCGA, NAKSM-SAM, NAKSM-SCA, NAKSM-SGA, NAKSM-SCGA, SKSM-SAM, SKSM-SCA, SKSM-SGA, and SKSM-SCGA.

Qualitatively, it can be inferred from Figure 6 that the mineral mapping results based on KSM are more contiguous and extensive than those of SM, no matter which matching or mapping method was used. In particular, for the three KSM mapping methods, NKSM lost a number of calcite and muscovite samples compared with NAKSM and SKSM. For SAM and SCA, NAKSM and SKSM have similar mineral mapping results. For SGA and SCGA, SKSM identifies more chalcedony than NKSM and NAKSM. Furthermore, among the four matching methods, SGA and SCGA can identify more calcite and muscovite samples than SAM and SCA.

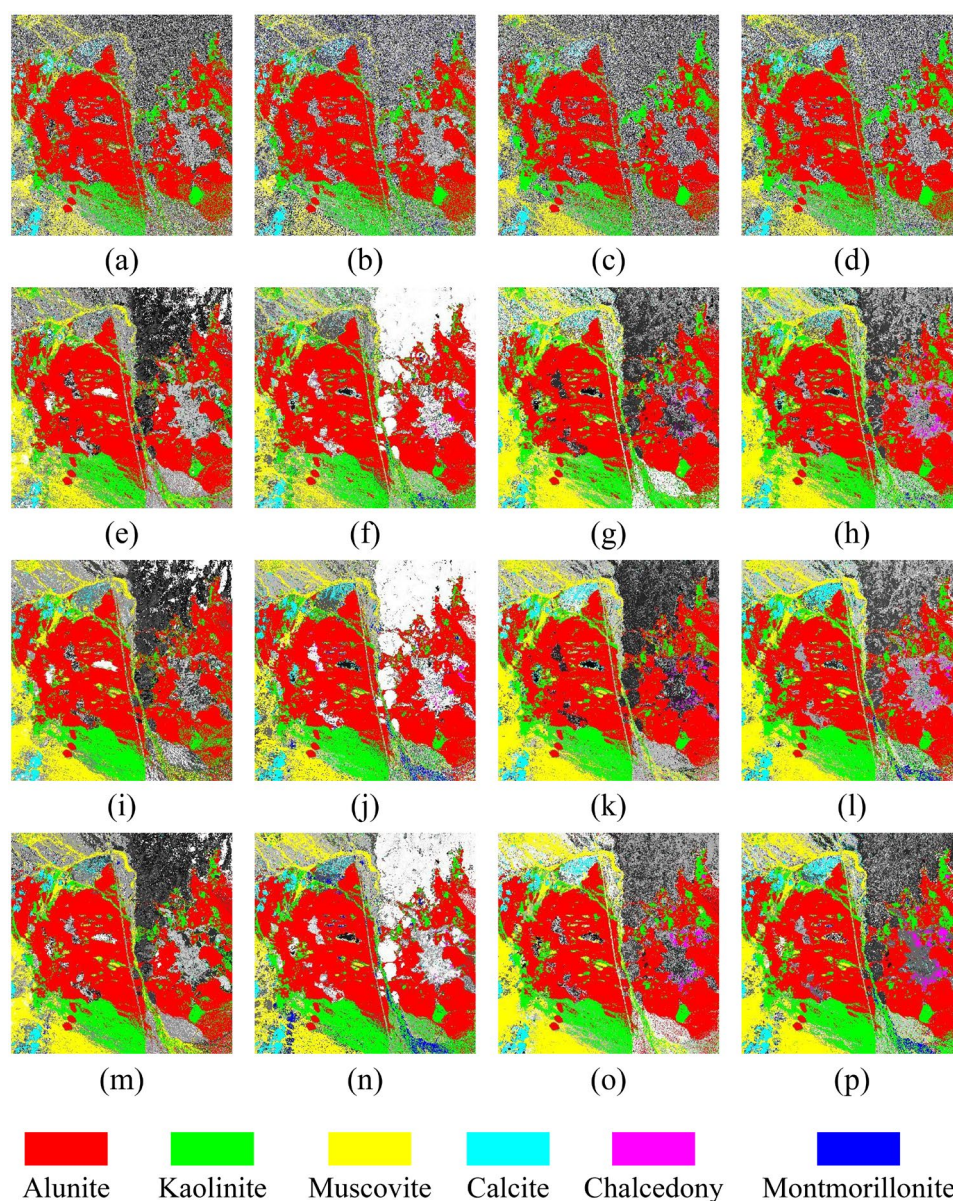


Figure 6. Mineral mapping results of the AVIRIS image: (a–d) are the mapping results based on SM–SAM, SM–SCA, SM–SGA, and SM–SCGA, respectively; (e–h) are the mapping results based on NKSM–SAM, NKSM–SCA, NKSM–SGA, and NKSM–SCGA, respectively; (i–l) are the mapping results based on NAKSM–SAM, NAKSM–SCA, NAKSM–SGA, and NAKSM–SCGA, respectively; and (m–p) are the mapping results based on SKSM–SAM, SKSM–SCA, SKSM–SGA, and SKSM–SCGA, respectively.

Figure 7 displays the accuracy assessment of the 254 mineral mapping results of the AVIRIS image, in which the horizontal axis represents the number of clustering, and the vertical axis represents OA. Quantitatively, it can be seen that KSM performs much better than SM for any initial cluster center or matching method. Specifically, NAKSM and SKSM outperform NKSM, no matter which matching method was used. For SAM and SCA, NAKSM and SKSM have similar mineral mapping accuracies. For SGA and SCGA, the OA curves of SKSM are above those of NAKSM. Furthermore, among the four matching methods, SAM and SCA have similar mapping accuracies, which are less than those of SGA and SCGA. In addition, for each mapping method, SCGA performs slightly better than SGA in OA.

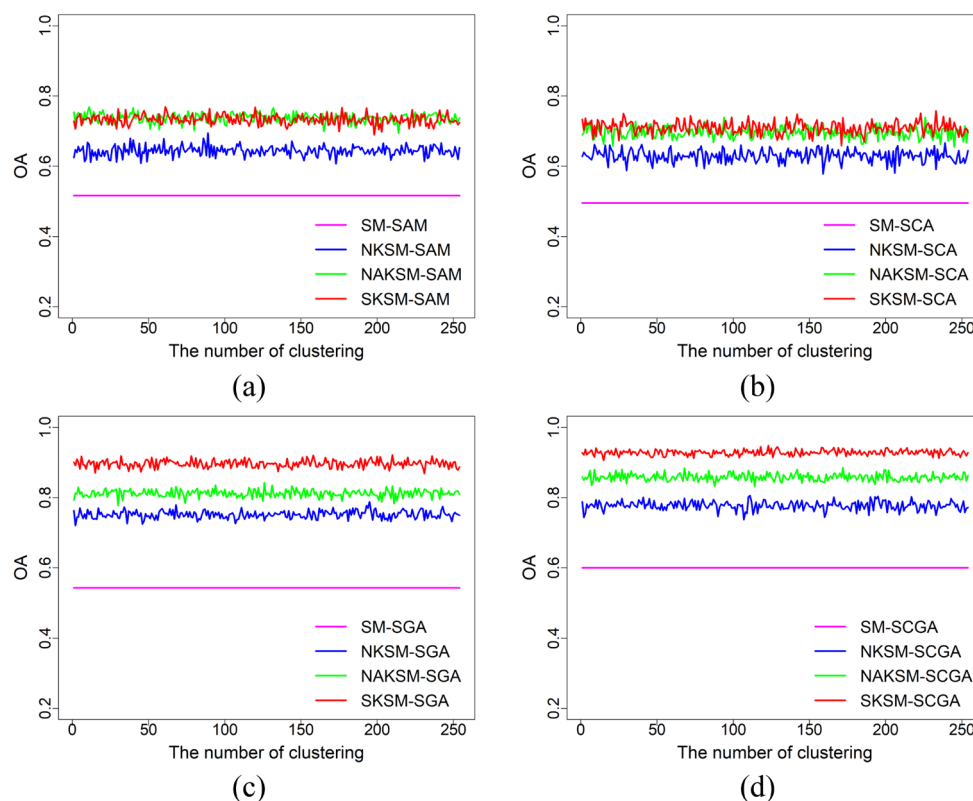


Figure 7. Mineral mapping accuracies of the AVIRIS image: (a–d) are the mapping accuracies based on SAM, SCA, SGA, and SCGA, respectively.

In terms of the average mineral mapping accuracies of the AVIRIS image, it can be inferred from Table 1 that, for each matching method, any KSM mapping method outperforms SM. Specifically, for SAM and SCA, although NKSM performs worse than NAKSM and SKSM, its average mapping accuracies are still about 13% higher than SM. For NAKSM and SKSM, the average mapping accuracies of SAM and SCA are about 22%, 20%, 22%, and 22% higher than SM, respectively. For SGA and SCGA, SKSM outperforms NKSM and NAKSM, and its average overall accuracies are about 35% and 33% higher than SM, while the average mapping accuracies of SGA and SCGA based on NKSM and NAKSM are about 21%, 18%, 27%, and 26% higher than SM, respectively. Among the three KSM mapping methods, the average mapping accuracy of SKSM is about 15% and 9% higher than those of NKSM and NAKSM at most. For each mapping method, SCGA outperforms other matching methods in OA. In addition, SKSM–SCGA has higher average accuracies than other classifiers.

Table 1. Average mineral mapping accuracies of the AVIRIS image.

Matching Method	SM	NKSM	NAKSM	SKSM
SAM	0.5167	0.6441	0.7375	0.7329
SCA	0.4955	0.6296	0.6954	0.7102
SGA	0.5431	0.7517	0.8120	0.8966
SCGA	0.6005	0.7772	0.8580	0.9282

To analyze the mineral mapping performance of various matching methods under different SNRs, zero-mean Gaussian noise with different standard deviations was added to the AVIRIS image. The higher the noise standard deviation, the lower the SNR. Qualitatively, as shown in Figure 8, KSM performs significantly better than SM in mineral mapping. Moreover, it can be inferred from Figures 6 and 8 that, among the four matching methods, the mineral mapping results of SCA and SCGA change the least after adding

noise, while the mineral mapping performances of SAM and SGA are obviously limited by noise. Specifically, before adding noise, SM-SGA has better mapping results than SM-SAM and SM-SCA, while after adding noise to the AVIRIS image, SM-SGA performs worst among the four SM classifiers and only gets some alunite, kaolinite, and little calcite. Although the mapping results of SM-SGA in Figure 8 are greatly improved by KSM, SGA-based KSM classifiers still perform worse than the KSM classifiers using SCA and SCGA. Similarly, despite that KSM improves the mapping results of SM-SAM to some extent, after adding noise, SAM-based KSM classifiers perform worse than the KSM classifiers using other matching methods. Unlike SAM and SGA, after adding noise to the AVIRIS image, SCA and SCGA retain most of the mineral mapping results in Figure 6 and show similar mapping performance.

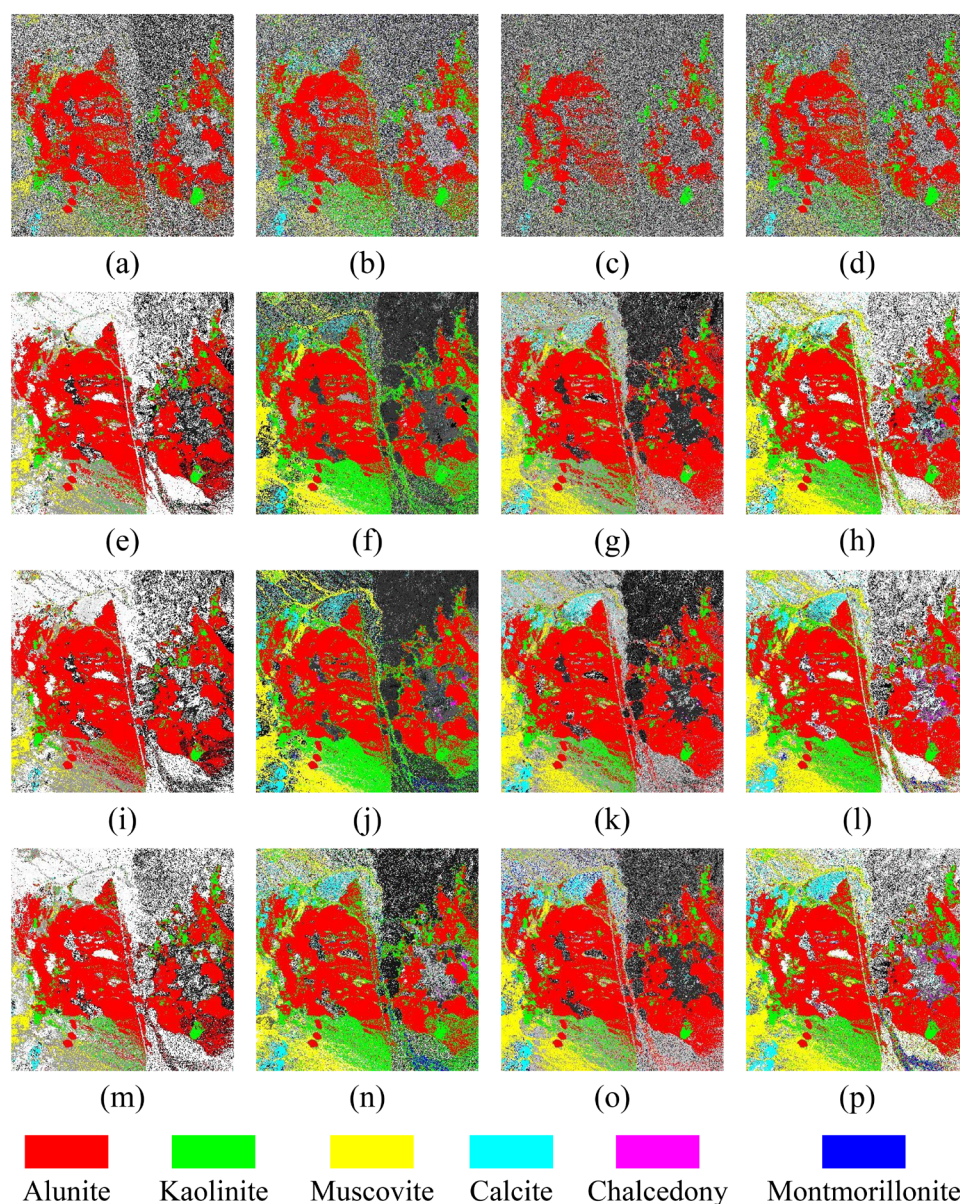


Figure 8. Mineral mapping results of the AVIRIS image after adding zero-mean Gaussian noise with the standard deviation of 0.006: (a–d) are the mapping results based on SM-SAM, SM-SCA, SM-SGA, and SM-SCGA, respectively; (e–h) are the mapping results based on NKSM-SAM, NKSM-SCA, NKSM-SGA, and NKSM-SCGA, respectively; (i–l) are the mapping results based on NAKSM-SAM, NAKSM-SCA, NAKSM-SGA, and NAKSM-SCGA, respectively; and (m–p) are the mapping results based on SKSM-SAM, SKSM-SCA, SKSM-SGA, and SKSM-SCGA, respectively.

Figure 9 shows the mineral mapping accuracies of the AVIRIS image after adding zero-mean Gaussian noise, in which the horizontal axis represents the noise standard deviation with unequal-interval distribution. Quantitatively, for SM, SGA generally performs worse than other matching methods; for KSM, the OA curves of SAM are below those of other matching methods when the noise standard deviation is greater than about 0.003. For SM and KSM, SCA has higher mapping accuracies than SAM and SGA in the noise standard deviation range of about 0.006 to 0.01. In addition, for any mapping method, the OA curves of SCGA are always above those of SGA, which means SCGA can effectively improve the mapping accuracy of SGA.

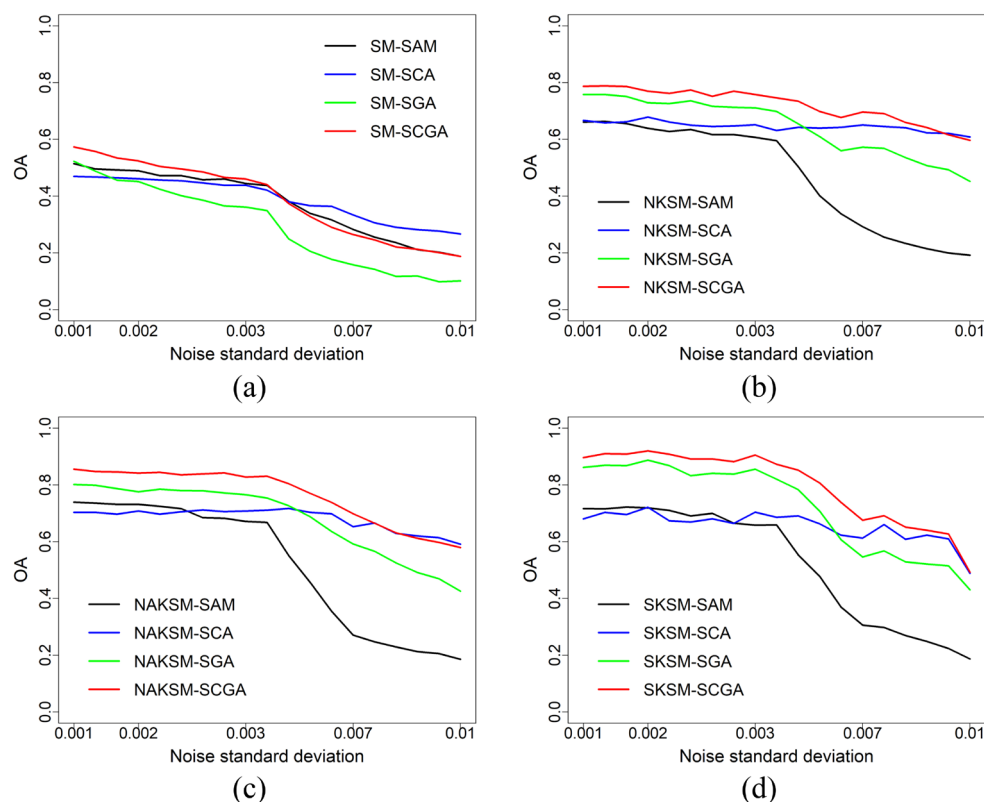


Figure 9. Mineral mapping accuracies of the AVIRIS image after adding zero-mean Gaussian noise: (a–d) are the mapping accuracies based on SM, NKSM, NAKSM, and SKSM, respectively.

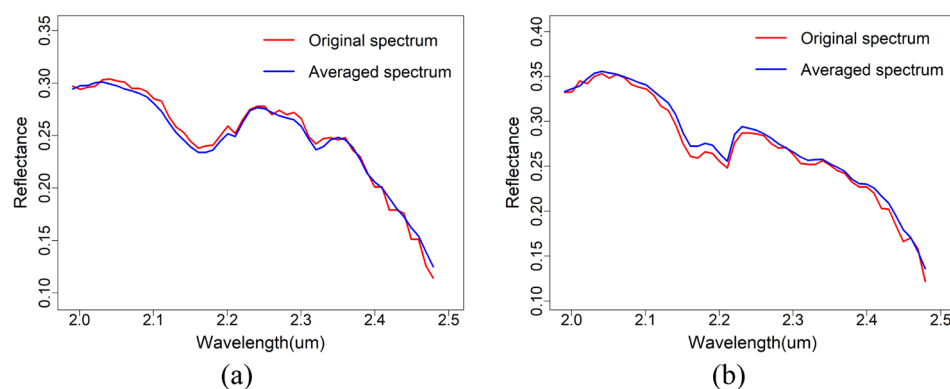
Table 2 shows the average mineral mapping time of different classifiers, which is obtained under the same conditions. It can be seen that, in terms of the total mapping time, SM takes more than 71 min to complete the four matching processes, while NKSM, NAKSM, and SKSM only need about 7, 10, and 6 min to obtain much better mineral mapping results, respectively. Specifically, for SAM, NKSM, NAKSM, and SKSM save about 51%, 33%, and 57% of the mapping time; for SCA, the mapping time of NKSM, NAKSM, and SKSM only accounts for 6%, 8%, and 5% of the mapping time of SM, respectively; for SGA, 48%, 28%, and 54% of the mapping time is saved by the three KSM mapping methods; for SCGA, NKSM, NAKSM, and SKSM save about 95%, 93%, and 96% of the mapping time, respectively. Furthermore, through clustering-matching, the mineral mapping efficiency of SCA and SCGA is improved much more than that of SAM and SGA, which have similar performance in mineral mapping time. Moreover, NAKSM takes at least 36 s more than NKSM to complete the clustering-matching process. In addition, for each matching method, the mineral mapping time of SKSM is less than NKSM and NAKSM. Compared with NKSM and NAKSM, SKSM saves about 12% and 38% of the total mapping time, respectively.

Table 2. Average mineral mapping time of SM and KSM.

Time (sec)	SM	NKSM	NAKSM	SKSM
SAM	201.8196	99.5971	136.1710	86.7398
SCA	1812.1085	102.4428	142.2040	90.5664
SGA	187.2481	97.6556	134.8296	85.6867
SCGA	2079.9541	104.1109	155.0557	92.2011
Total	4281.1302	403.8064	568.2603	355.1941

5. Discussion

In terms of mineral mapping accuracy, KSM outperforms SM, and even the minimum overall accuracies of KSM are higher than those of SM. This occurs because the noise in the pixel spectrum can be removed to some extent by averaging, and the cluster centers of k-means are exactly updated by averaging. As shown in Figure 10, averaging not only smooths the spectral curves of alunite and kaolinite, but it also preserves their spectral absorption features. Among the three KSM mapping methods, NKSM performs worse than NAKSM and SKSM in OA, because the W and H matrices initialized by NNDSVD contain a number of zeros, which has a certain impact on its clustering-matching results. By replacing zeros with the average of all elements of the AVIRIS image, NAKSM has a higher mapping accuracy than NKSM. However, since this ensemble average may lose the distribution of some minerals with fewer pixels, the NAKSM classifiers using SGA and SCGA lost some chalcedony samples and have worse mapping accuracies than the corresponding SKSM classifiers.

**Figure 10.** Original and averaged spectrum of (a) alunite and (b) kaolinite.

KSM also performs much better than SM in mineral mapping efficiency, despite the fact that the algorithm complexity of KSM is greater than that of SM. Compared with SM, KSM can save more than 95% of the mapping time. This is because KSM uses the cluster centers to match the spectral library, rather than using per-pixel matching, and K (i.e., 481) is much less than the pixel number (i.e., 122,500) of the AVIRIS image. Moreover, the fast-clustering ability of k-means also contributes to the improvement of mapping efficiency. Due to the sparsity of NNDSVD, the mapping efficiency of NKSM is higher than that of NAKSM. In addition, since SMNMF does not require matrix factorization and only needs to find several pixels to initialize the H matrix, while NNDSVD and NNDSVDa need two SVD processes, SKSM outperforms NKSM and NAKSM in mapping efficiency. Therefore, it can be said that SMNMF is a simple and effective NMF initialization method. Nevertheless, since SMNMF uses SM to initialize the coefficient matrix, it needs the support of a spectral library.

Figure 11 shows the average overall accuracies of 20 random clustering-matchings of KSM with different K values. It can be seen that, for each KSM mapping method, with the increase of K, the average overall accuracies of the four matching methods gradually increase, and the mapping accuracy at K = 481 is much higher than that at K = 6. Therefore,

for k-means clustering, setting K to the spectral curve number of the USGS mineral spectral library or larger is conducive to improving its mineral mapping accuracy.

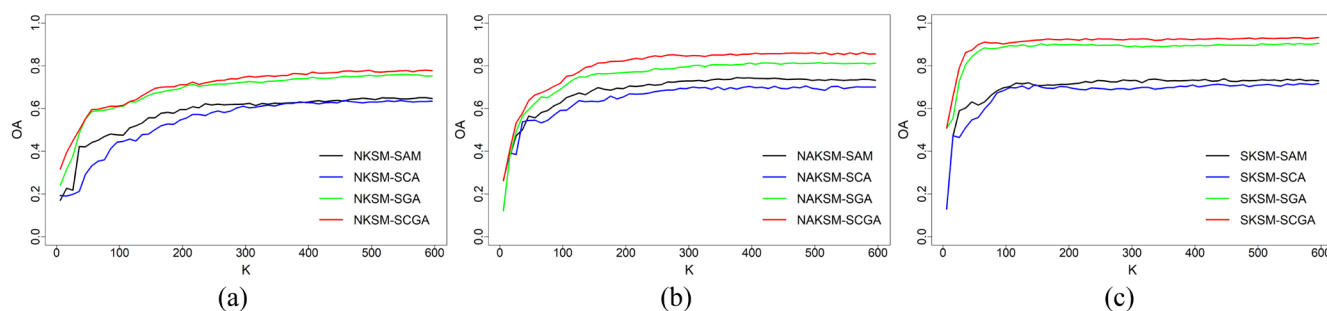


Figure 11. Average overall accuracies of 20 random clustering-matchings of KSM with different K values: (a–c) are the mapping accuracies based on NKSM, NAKSM, and SKSM, respectively.

In terms of the four matching methods, Figure 7 and Table 1 show that SGA has higher mapping accuracies than SAM and SCA for the original AVIRIS image, denoting that shape similarity can accurately reflect the spectral differences of fine objects when SNR is high enough. However, as shown in Figures 8 and 9, SM–SGA demonstrates worse mapping performance than do SM–SAM and SM–SCA when SNR is lower, which means that SGA is more sensitive to noise than SAM and SCA. This is the case because SGA calculates the reflectivity difference when obtaining the shape similarity between two spectral vectors. Furthermore, Figure 9 shows that SCA outperforms SAM and SGA in mineral mapping at low SNR, indicating that, through decentralization, SCA can reduce the influence of noise on matching accuracy. By combining the correlation and shape similarity of two spectral curves, SCGA has slightly higher mapping accuracies than SGA at high SNR, and it shows a similar mapping performance with SCA at low SNR. That is, the two variants of SAM (i.e., SGA and SCA) demonstrate good mapping performance at high and low SNR, respectively, while their combination (i.e., SCGA) could achieve promising mapping results at both high and low SNR.

It is well-known that mean filtering (MF) also removes noise from images by averaging. The difference between KSM and MF is that KSM can ensure that the pixels used to calculate the average are of the same type, while MF cannot guarantee this. Compared with KSM, MF has three undeniable shortcomings in mineral mapping. One is that averaging the pixel values of different mineral types will render the MF mapping results fuzzy. Figure 12 shows the mineral mapping results of the AVIRIS image based on MF, whose window length is set as 3. It can be inferred from Figures 6 and 12 that, compared with KSM, MF blurs out the details of the mineral mapping results, indicating that it is not the averaging but the averaging of the pixel values of different types that makes the mapping results fuzzy.

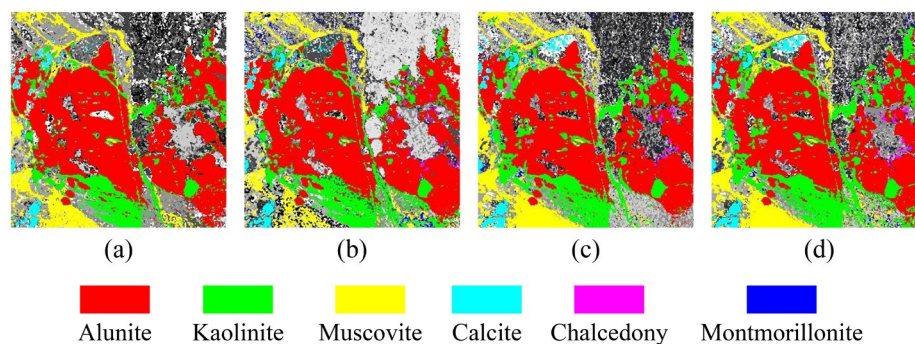


Figure 12. Mineral mapping results of the AVIRIS image based on MF: (a–d) are the mapping results of SAM, SCA, SGA, and SCGA, respectively.

Another shortcoming of MF in mineral mapping is that the mixing of different mineral types in the filtering window will pose a great influence on its mineral mapping accuracies. The more kinds of minerals in the filtering window, the higher the mixing level. In order to analyze the influence of the mixing of various mineral types on the mapping results of KSM and MF, 30 AVIRIS images with different mixing levels were achieved using an iterative procedure. In each iteration, the positions of 4000 pixels of the AVIRIS image were randomly exchanged to make the mineral types within the 3×3 filtering window inconsistent. The mixing level of these AVIRIS images increases as the iteration progresses. Quantitatively, it can be seen from Figure 13 that, for each matching method, with the increase of mixing level, the mapping accuracy of MF decreases gradually. This occurs because the mixing of different mineral types causes the average spectrum of MF to be unable to accurately represent the spectral features of the middle pixel in the filtering window, which results in a matching error. The OA of KSM remains stable at the same level, no matter which matching or mapping method is used. That is, the mapping results of KSM are independent of the mixing of different mineral types because it can take the average of the same mineral type by clustering. Furthermore, compared with KSM, MF demonstrates lower mapping efficiency because of its per-pixel matching method.

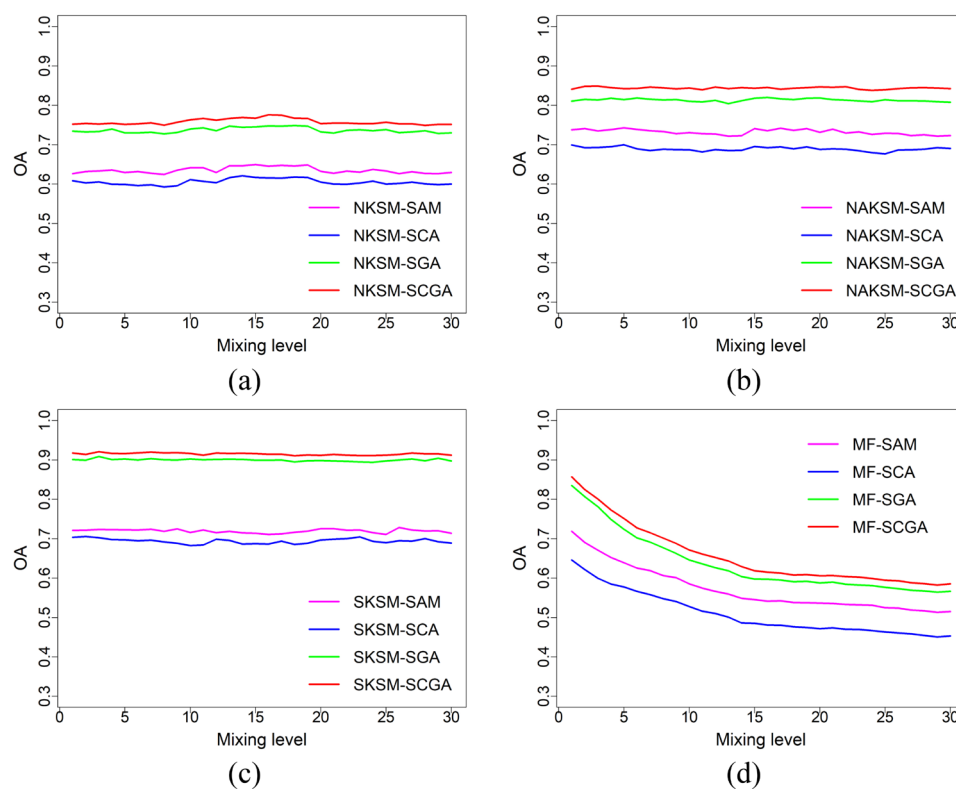


Figure 13. Mineral mapping accuracies of 30 AVIRIS images with different mixing levels: (a–d) are the mapping accuracies based on NKSM, NAKSM, SKSM, and MF, respectively.

Considering that k-means falls easily into the local optimal solution, a clustering algorithm with global search ability, such as genetic algorithm, simulated annealing algorithm, and particle swarm optimization, can be used in clustering-matching to further improve the mapping accuracy. However, as previously mentioned, complex clustering algorithms may reduce the mapping efficiency of clustering-matching. In addition, despite the good mineral mapping results achieved by the proposed KSM mapping approach, the dependence of clustering-matching on the spectral library may limit its application.

6. Conclusions

This work proposes an unsupervised clustering-matching mapping idea and combines k-means and SM for hyperspectral mineral mapping. The experimental results show that this combination could effectively reduce the fragmentation of the matching results and greatly improve mapping efficiency compared with that of traditional spectral matching technology. The average mineral mapping accuracy of KSM is about 35% higher than that of SM at most, and more than 95% of the mapping time can be saved, denoting that clustering-matching is an efficient, unsupervised mineral mapping method. During the clustering-matching process, the following conclusions can be addressed as well:

- In feature extraction, the proposed NMF initialization method based on SM performs better than the widely used matrix factorization initialization method in mapping accuracy and efficiency.
- For k-means clustering, setting K to the spectral curve number of a mineral spectral library or larger can effectively improve the mineral mapping accuracy of clustering-matching.
- In terms of the four matching methods, the proposed combined matching method can achieve promising mapping results at both high and low signal-to-noise ratios.
- In noise reduction, although both KSM and mean filtering remove noise by averaging, KSM does not blur out the details of the mineral mapping results and has a greater mapping efficiency. Most importantly of all, KSM is independent of the mixing of different mineral types.

Our work here may not only be helpful for autonomous mineral mapping, but it may also provide reference for the rapid and autonomous identification of other fine objects. Future research on more efficient clustering algorithms may help further improve the mapping results.

Author Contributions: Conceptualization and methodology, Z.R. and L.S.; validation, resources, and writing—original draft preparation, Z.R.; formal analysis and supervision, L.S.; software, writing—review and editing, project administration, and funding acquisition, Q.Z. All authors have read and agreed to the published version of the manuscript.

Funding: This research was funded by National Key Research and Development Program, grant number 2019YFE0126700, and Shandong Provincial Natural Science Foundation, grant number ZR2020QD018.

Institutional Review Board Statement: Not applicable.

Informed Consent Statement: Not applicable.

Data Availability Statement: Publicly available datasets were analyzed in this study. This data can be found here: [http://www.ehu.eus/ccwintco/index.php?title=Hyperspectral_Remote_Sensing_Scenes].

Conflicts of Interest: The authors declare no conflicts of interest.

Abbreviations

The number of cluster centers	K
Spectral angle mapper	SAM
Spectral correlation angle	SCA
Spectral gradient angle	SGA
The matching method combing SCA and SGA	SCGA
Band depth	BD
Nonnegative matrix factorization	NMF
Singular value decomposition	SVD
Nonnegative Double Singular Value Decomposition	NNDSVD
The variant of NNDSVD	NNDSVDa

The NMF initialization method using spectral matching technology	SMNMF
Spectral matching	SM
The combination of k-means and SM	KSM
KSM mapping method based on NNDSVD	NKSM
KSM mapping method based on NNDSVDa	NAKSM
KSM mapping method based on SMNMF	SKSM

References

- Ouahabi, M.E.; Daoudi, L.; Fagel, N. Mineralogical and geotechnical characterization of clays from northern Morocco for their potential use in the ceramic industry. *Clay Miner.* **2014**, *49*, 35–51. <https://doi.org/10.1180/claymin.2014.049.1.04>.
- Hojamberdiev, M.; Eminov, A.; Xu, Y. Utilization of muscovite granite waste in the manufacture of ceramic tiles. *Ceram. Int.* **2011**, *37*, 871–876. <https://doi.org/10.1016/j.ceramint.2010.10.032>.
- Cordell, D.; Drangert, J.O.; White, S. The story of phosphorus: Global food security and food for thought. *Glob. Environ. Chang.* **2009**, *19*, 292–305. <https://doi.org/10.1016/j.gloenvcha.2008.10.009>.
- Laakso, K.; Middleton, M.; Heinig, T.; Bärts, R.; Lintinen, P. Assessing the ability to combine hyperspectral imaging (HSI) data with Mineral Liberation Analyzer (MLA) data to characterize phosphate rocks. *Int. J. Appl. Earth Obs. Geoinf.* **2018**, *69*, 1–12. <https://doi.org/10.1016/j.jag.2018.02.018>.
- Li, W.; Zhao, W.; Hu, Q. Effect of bifid triple viable tablets combined with montmorillonite powder on pediatric diarrhea and its influence on children's immune function. *Chin. Pediatr. Integr. Tradit. West. Med.* **2018**, *2*, 150–152. <https://doi.org/10.3969/j.issn.1674-3865.2018.02.018>.
- Ni, L.; Xu, H.; Zhou, X. Mineral Identification and Mapping by Synthesis of Hyperspectral VNIR/SWIR and Multispectral TIR Remotely Sensed Data with Different Classifiers. *IEEE J. Sel. Top. Appl. Earth Observ. Remote Sens.* **2020**, *13*, 3155–3163. <https://doi.org/10.1109/JSTARS.2020.2999057>.
- Vane, G.; Goetz, A.F.H. Terrestrial imaging spectrometry: Current status, future trends. *Remote Sens. Environ.* **1993**, *44*, 117–126. [https://doi.org/10.1016/0034-4257\(93\)90011-L](https://doi.org/10.1016/0034-4257(93)90011-L).
- Hubbard, B.E.; Crowley, J.K.; Zimbelman, D.R. Comparative alteration mineral mapping using visible to shortwave infrared (0.4–2.4 μm) Hyperion, ALI, and ASTER imagery. *IEEE Trans. Geosci. Remote Sens.* **2003**, *41*, 1401–1410. <https://doi.org/10.1109/TGRS.2003.812906>.
- Meer, F.V.D.; Bakker, W. Cross correlation spectral matching: Application to surface mineralogical mapping using AVIRIS data from cuprite, Nevada. *Remote Sens. Environ.* **1997**, *61*, 371–382. [https://doi.org/10.1016/S0034-4257\(97\)00047-3](https://doi.org/10.1016/S0034-4257(97)00047-3).
- Yi, C.; Zhao, Y.Q.; Chan, J.C. Spectral Super-Resolution for Multispectral Image Based on Spectral Improvement Strategy and Spatial Preservation Strategy. *IEEE Trans. Geosci. Remote Sens.* **2019**, *57*, 9010–9024. <https://doi.org/10.1109/TGRS.2019.2924096>.
- Acosta, I.C.C.; Khodadadzadeh, M.; Gloaguen, R. Resolution Enhancement for Drill-Core Hyperspectral Mineral Mapping. *Remote Sens.* **2021**, *13*, 2296. <https://doi.org/10.3390/rs13122296>.
- Tompolidi, A.-M.; Sykioti, O.; Koutroumbas, K.; Parcharidis, I. Spectral Unmixing for Mapping a Hydrothermal Field in a Volcanic Environment Applied on ASTER, Landsat-8/OLI, and Sentinel-2 MSI Satellite Multispectral Data: The Nisyros (Greece) Case Study. *Remote Sens.* **2020**, *12*, 4180. <https://doi.org/10.3390/rs12244180>.
- Jain, R.; Sharma, R.U. Airborne hyperspectral data for mineral mapping in Southeastern Rajasthan, India. *Int. J. Appl. Earth Obs. Geoinf.* **2019**, *81*, 137–145. <https://doi.org/10.1016/j.jag.2019.05.007>.
- Cui, B.; Cui, J.; Hao, S.; Guo, N.; Lu, Y. Spectral-spatial Hyperspectral Image Classification Based on Superpixel and Multi-classifier Fusion. *Int. J. Remote Sens.* **2020**, *41*, 6157–6182. <https://doi.org/10.1080/01431161.2020.1736730>.
- Kang, X.; Duan, P.; Xiang, X.; Li, S.; Benediktsson, J.A. Detection and Correction of Mislabeled Training Samples for Hyperspectral Image Classification. *IEEE Trans. Geosci. Remote Sens.* **2018**, *56*, 5673–5686. <https://doi.org/10.1109/TGRS.2018.2823866>.
- Hughes, G. On the mean accuracy of statistical pattern recognizers. *IEEE Trans. Inf. Theory.* **1968**, *14*, 55–63. <https://doi.org/10.1109/TIT.1968.1054102>.
- Paoletti, M.E.; Haut, J.M.; Fernandez-Beltran, R.; Plaza, J.; Plaza, A.J.; Pla, F. Deep Pyramidal Residual Networks for Spectral-Spatial Hyperspectral Image Classification. *IEEE Trans. Geosci. Remote Sens.* **2019**, *57*, 740–754. <https://doi.org/10.1109/TGRS.2018.2860125>.
- Iordache, M.; Bioucas-Dias, J.M.; Plaza, A. Collaborative Sparse Regression for Hyperspectral Unmixing. *IEEE Trans. Geosci. Remote Sens.* **2014**, *52*, 341–354. <https://doi.org/10.1109/TGRS.2013.2240001>.
- Zhang, B.; Sun, X.; Gao, L.; Yang, L. Endmember Extraction of Hyperspectral Remote Sensing Images Based on the Ant Colony Optimization (ACO) Algorithm. *IEEE Trans. Geosci. Remote Sens.* **2011**, *49*, 2635–2646. <https://doi.org/10.1109/TGRS.2011.2108305>.

20. Chan, T.; Ma, W.; Ambikapathi, A.; Chi, C. A Simplex Volume Maximization Framework for Hyperspectral Endmember Extraction. *IEEE Trans. Geosci. Remote Sens.* **2011**, *49*, 4177–4193. <https://doi.org/10.1109/TGRS.2011.2141672>.
21. Dennison, P.E.; Halligan, K.Q.; Roberts, D.A. A comparison of error metrics and constraints for multiple endmember spectral mixture analysis and spectral angle mapper. *Remote Sens. Environ.* **2004**, *93*, 359–367. <https://doi.org/10.1016/j.rse.2004.07.013>.
22. Meer, F.V.D.; Bakker, W. CCSM: Cross Correlogram Spectral Matching. *Int. J. Remote Sens.* **1997**, *18*, 1197–1201. <https://doi.org/10.1080/014311697218674>.
23. Meer, F.V.D. The effectiveness of spectral similarity measures for the analysis of hyperspectral imagery. *Int. J. Appl. Earth Obs. Geoinf.* **2006**, *8*, 3–17. <https://doi.org/10.1016/j.jag.2005.06.001>.
24. Kumar, A.S.; Keerthi, V.; Manjunath, A.S.; Werff, H.V.D.; Meer, F.V.D. Hyperspectral image classification by a variable interval spectral average and spectral curve matching combined algorithm. *Int. J. Appl. Earth Obs. Geoinf.* **2010**, *12*, 261–269. <https://doi.org/10.1016/j.jag.2010.03.004>.
25. Tzortzis, G.; Likas, A. The minmax k-means clustering algorithm. *Pattern Recognit.* **2014**, *47*, 2505–2516. <https://doi.org/10.1016/j.patcog.2014.01.015>.
26. Filippone, M.; Camastra, F.; Masulli, F.; Rovetta, S. A survey of kernel and spectral methods for clustering. *Pattern Recognit.* **2008**, *41*, 176–190. <https://doi.org/10.1016/j.patcog.2007.05.018>.
27. Tompolidi, A.; Sykioti, O.; Koutroumbas, K.; Parcharidis, I. Detection of hydrothermal alteration on volcanic environments applying clustering on Landsat 8 OLI data. Case study: The Nisyros caldera (Greece). In Proceedings of the Conference HGS 2019: 12th International Conference of the Hellenic Geographical Society, Athens, Greece, 1–4 November 2019. <https://doi.org/10.13140/RG.2.2.19110.88648>.
28. Klein, M.P.; Barton, G.W. Enhancement of signal-to-noise ratio by continuous averaging: Application to magnetic resonance. *Rev. Sci. Instrum.* **2004**, *34*, 754–759. <https://doi.org/10.1063/1.1718564>.
29. Micciancio, S. Noise reduction by averaging over the optical path in interferometry. *Infrared Phys. Technol.* **1977**, *17*, 67–70. [https://doi.org/10.1016/0020-0891\(77\)90097-5](https://doi.org/10.1016/0020-0891(77)90097-5).
30. Manning, B.R.; Cochran, C.J.; Lenahan, P.M. An improved adaptive signal averaging technique for noise reduction and tracking enhancements in continuous wave magnetic resonance. *Rev. Sci. Instrum.* **2020**, *91*, 033106. <https://doi.org/10.1063/1.5123600>.
31. Deledalle, C.A.; Denis, L.; Tupin, F. NL-InSAR: Nonlocal Interferogram Estimation. *IEEE Trans. Geosci. Remote Sens.* **2011**, *49*, 1441–1452. <https://doi.org/10.1109/TGRS.2010.2076376>.
32. Rodger, A.; Fabris, A.; Laukamp, C. Feature Extraction and Clustering of Hyperspectral Drill Core Measurements to Assess Potential Lithological and Alteration Boundaries. *Minerals* **2021**, *11*, 136. <https://doi.org/10.3390/min11020136>.
33. Martel, E.; Lazcano, R.; López, J.; Madroñal, D.; Salvador, R.; López, S.; Juárez, E.; Guerra, R.; Sanz, C.; Sarmiento, R. Implementation of the Principal Component Analysis onto High-Performance Computing Facilities for Hyperspectral Dimensionality Reduction: Results and Comparisons. *Remote Sens.* **2018**, *10*, 864. <https://doi.org/10.3390/rs10060864>.
34. Nielsen, A.A. Kernel Maximum Autocorrelation Factor and Minimum Noise Fraction Transformations. *IEEE Trans. Image Process.* **2011**, *20*, 612–624. <https://doi.org/10.1109/TIP.2010.2076296>.
35. Gao, L.; Zhao, B.; Jia, X.; Liao, W.; Zhang, B. Optimized Kernel Minimum Noise Fraction Transformation for Hyperspectral Image Classification. *Remote Sens.* **2017**, *9*, 548. <https://doi.org/10.3390/rs9060548>.
36. Lee, D.D.; Seung, H.S. Learning the parts of objects by nonnegative matrix factorization. *Nature* **1999**, *401*, 788–791. <https://doi.org/10.1038/44565>.
37. Qiao, H. New SVD based initialization strategy for Nonnegative Matrix Factorization. *Pattern Recognit. Lett.* **2015**, *63*, 71–77. <https://doi.org/10.1016/j.patrec.2015.05.019>.
38. Wild, S.; Curry, J.; Dougherty, A. Improving nonnegative matrix factorizations through structured initialization. *Pattern Recognit.* **2004**, *37*, 2217–2232. <https://doi.org/10.1016/j.patcog.2004.02.013>.
39. Gong, L.; Nandi, A.K. An enhanced initialization method for non-negative matrix factorization. In Proceedings of the 2013 IEEE International Workshop on Machine Learning for Signal Processing (MLSP), Southampton, UK, 22–25 September 2013. <https://doi.org/10.1109/MLSP.2013.6661949>.
40. Li, T.; Ding, C. The Relationships Among Various Nonnegative Matrix Factorization Methods for Clustering. In Proceedings of the Sixth International Conference on Data Mining, Hong Kong, China, 18–22 December 2006; pp. 362–371. <https://doi.org/10.1109/ICDM.2006.160>.
41. Resmini, R.G.; Kappus, M.E.; Aldrich, W.S.; Harsanyi, J.C.; Anderson, M. Mineral mapping with Hyperspectral Digital Imagery Collection Experiment (HYDICE) sensor data at Cuprite, Nevada, U.S.A. *Int. J. Remote Sens.* **1997**, *18*, 1553–1570. <https://doi.org/10.1080/014311697218278>.
42. Siebels, K.; Gota, K.; Germain, M. Estimation of Mineral Abundance from Hyperspectral Data Using a New Supervised Neighbor-Band Ratio Unmixing Approach. *IEEE Trans. Geosci. Remote Sens.* **2020**, *58*, 6754–6766. <https://doi.org/10.1109/TGRS.2020.2969577>.
43. Clark, R.N.; Swayze, G.A.; Livo, K.E.; Kokaly, R.F.; Sutly, S.J.; Dalton, J.B.; McDougal, R.R.; Gent, C.A. Imaging spectroscopy: Earth and planetary remote sensing with the USGS Tetracorder and expert systems. *J. Geophys. Res. Atmos.* **2003**, *108*, 5131. <https://doi.org/10.1029/2002JE001847>.
44. Chen, X.; Warner, T.A.; Campagna, D.J. Integrating visible, near-infrared and short-wave infrared hyperspectral and multispectral thermal imagery for geological mapping at cuprite, Nevada. *Remote Sens. Environ.* **2007**, *110*, 344–356. <https://doi.org/10.1016/j.rse.2007.03.015>.

45. Green, R.O.; Eastwood, M.L.; Sarture, C.M.; Chrien, T.G.; Aronsson, M.; Chippendale, B.J.; Faust, J.A.; Pavri, B.E.; Chovit, C.J.; Solis, M.; et al. Imaging Spectroscopy and the Airborne Visible/Infrared Imaging Spectrometer (AVIRIS). *Remote Sens. Environ.* **1998**, *65*, 227–248. [https://doi.org/10.1016/S0034-4257\(98\)00064-9](https://doi.org/10.1016/S0034-4257(98)00064-9).
46. Kruse, F.A.; Boardman, J.W.; Huntington, J.F. Comparison of airborne hyperspectral data and EO-1 Hyperion for mineral mapping. *IEEE Trans. Geosci. Remote Sens.* **2003**, *41*, 1388–1400. <https://doi.org/10.1109/TGRS.2003.812908>.
47. Carvalho, O.A.D.; Carvalho, A.P.F.; Guimaraes, R.F.; Lopes, R.A.S.; Guimaraes, P.A.; Martins, E.D.S.; Pedreno, J.N. Classification of hyperspectral image using SCM methods for geobotanical analysis in the Brazilian savanna region. In Proceedings of the IEEE International Symposium on Geoscience and Remote Sensing (IGARSS), Toulouse, France, 21–25 July 2003. <https://doi.org/10.1109/IGARSS.2003.1295259>.
48. Ren, Z.; Sun, L.; Zhai, Q.; Liu, X. Mineral Mapping with Hyperspectral Image Based on an Improved K-Means Clustering Algorithm. In Proceedings of the IEEE International Symposium on Geoscience and Remote Sensing (IGARSS), Yokohama, Japan, 28 July–2 August 2019; pp. 2989–2992. <https://doi.org/10.1109/IGARSS.2019.8899113>.
49. Noomen, M.F.; Skidmore, A.K.; Meer, F.V.D.; Prins, H.H.T. Continuum removed band depth analysis for detecting the effects of natural gas, methane and ethane on maize reflectance. *Remote Sens. Environ.* **2006**, *105*, 262–270. <https://doi.org/10.1016/j.rse.2006.07.009>.
50. Sykioti, O.; Paronis, D.; Stagakis, S.; Kyparissis, A. Band depth analysis of chris/proba data for the study of a mediterranean natural ecosystem. correlations with leaf optical properties and ecophysiological parameters. *Remote Sens. Environ.* **2011**, *115*, 752–766. <https://doi.org/10.1016/j.rse.2010.11.003>.
51. Liu, X.; Xia, W.; Wang, B.; Zhang, L. An approach based on constrained nonnegative matrix factorization to unmix hyperspectral data. *IEEE Trans. Geosci. Remote Sens.* **2011**, *49*, 757–772. <https://doi.org/10.1109/TGRS.2010.2068053>.
52. Rezaei, M.; Boostani, R. An Efficient Initialization Method for Nonnegative Matrix Factorization. *Appl. Sci.* **2011**, *11*, 354–359. <https://doi.org/10.3923/jas.2011.354.359>.
53. Liu, H.W.; Li, X.L.; Zheng, X.Y. Solving nonnegative matrix factorization by alternating least squares with a modified strategy. *Data Min. Knowl. Discov.* **2013**, *26*, 435–451. <https://doi.org/10.1007/s10618-012-0265-y>.
54. Xue, Y.; Tong, C.S.; Chen, Y.; Chen, W.S. Clustering-based initialization for nonnegative matrix factorization. *Appl. Math. Comput.* **2008**, *205*, 525–536. <https://doi.org/10.1016/j.amc.2008.05.106>.
55. Zhao, L.; Zhang, G.; Xu, X. Facial expression recognition based on PCA and NMF. In *Intelligent Control and Automation*; Scientific Research Publishing: Wuhan, China, 2008; pp. 6826–6829. <https://doi.org/10.1109/WCICA.2008.4593968>.
56. Atif, S.M.; Qazi, S.; Gillis, N. Improved SVD-based initialization for nonnegative matrix factorization using low-rank correction. *Pattern Recognit. Lett.* **2019**, *122*, 53–59. <https://doi.org/10.1016/j.patrec.2019.02.018>.
57. Kitamura, D.; Ono, N. Efficient initialization for nonnegative matrix factorization based on nonnegative independent component analysis. In Proceedings of the 2016 IEEE International Workshop on Acoustic Signal Enhancement (IWAENC), Xi'an, China, 13–16 September 2016; pp. 1–5. <https://doi.org/10.1109/IWAENC.2016.7602947>.
58. Pompili, F.; Gillis, N.; Absil, P.A.; Glineur, F. Two algorithms for orthogonal nonnegative matrix factorization with application to clustering. *Neurocomputing* **2014**, *141*, 15–25. <https://doi.org/10.1016/j.neucom.2014.02.018>.
59. Li, X.; Cui, G.; Dong, Y. Graph Regularized Non-Negative Low-Rank Matrix Factorization for Image Clustering. *IEEE Trans. Cybern.* **2017**, *47*, 3840–3853. <https://doi.org/10.1016/10.1109/TCYB.2016.2585355>.
60. Boutsidis, C.; Gallopoulos, E. SVD based initialization: A head start for nonnegative matrix factorization. *Pattern Recognit.* **2008**, *41*, 1350–1362. <https://doi.org/10.1016/j.patcog.2007.09.010>.
61. Zhang, K.; Kwok, J.T. Clustered Nyström Method for Large Scale Manifold Learning and Dimension Reduction. *IEEE Trans. Neural Netw.* **2010**, *21*, 1576–1587. <https://doi.org/10.1109/TNN.2010.2064786>.
62. Du, H.; Wang, Y.; Duan, L. A New Method for Grayscale Image Segmentation Based on Affinity Propagation Clustering Algorithm. In Proceedings of the 2013 Ninth International Conference on Computational Intelligence and Security, Emeishan, China, 14–15 December 2013; pp. 170–173. <https://doi.org/10.1109/CIS.2013.42>.
63. Likas, A.; Vlassis, N.; Verbeek, J.J. The global k-means clustering algorithm. *Pattern Recognit.* **2003**, *36*, 451–461. [https://doi.org/10.1016/S0031-3203\(02\)00060-2](https://doi.org/10.1016/S0031-3203(02)00060-2).
64. Pena, J.M.; Lozano, J.A.; Larranaga, P. An empirical comparison of four initialization methods for the k-means algorithm. *Pattern Recognit. Lett.* **1999**, *20*, 1027–1040. [https://doi.org/10.1016/S0167-8655\(99\)00069-0](https://doi.org/10.1016/S0167-8655(99)00069-0).
65. Kumar, P.; Gupta, D.K.; Mishra, V.N.; Prasad, R. Comparison of Support Vector Machine, Artificial Neural Network, and Spectral Angle Mapper Algorithms for Crop Classification Using LISS IV Data. *Int. J. Remote Sens.* **2015**, *36*, 1604–1617. <https://doi.org/10.1080/2150704X.2015.1019015>.
66. Angelopoulou, E.; Lee, S.W.; Bajcsy, R. Spectral gradient: A material descriptor invariant to geometry and incident illumination. In Proceedings of the Seventh IEEE International Conference on Computer Vision, Kerkyra, Greece, 20–27 September 1999. <https://doi.org/10.1109/ICCV.1999.790312>.
67. Carvalho, O.A.; Meneses, P.R. Spectral Correlation Mapper (SCM): An Improvement on the Spectral Angle Mapper (SAM). In *Summaries of the Ninth Annual JPL Airborne Earth Science Workshop, February 23–25, 2000*; JPL: Pasadena, CA, USA, 2000.
68. Congalton, R.G. A review of assessing the accuracy of classifications of remotely sensed data. *Remote Sens. Environ.* **1991**, *37*, 35–46. [https://doi.org/10.1016/0034-4257\(91\)90048-B](https://doi.org/10.1016/0034-4257(91)90048-B).